AGU PUBLICATIONS

Geophysical Research Letters

RESEARCH LETTER
10.1002/2014GL062782

**Key Points:**
- The "hum" is caused by the interaction of ocean waves with the bottom slope
- Our model yields maps of seismic sources at all periods from 3 to 300 s
- Sources of the hum are strongest along shelf breaks, on the east side of oceans

**Supporting Information:**
- Text S1 and Figures S1–S4

**Correspondence to:**
F. Ardhuin,
ardhuin@ifremer.fr

**Citation:**
Ardhuin, F., L. Gualtieri, and E. Stutzmann (2015), How ocean waves rock the Earth: Two mechanisms explain microseisms with periods 3 to 300 s, *Geophys. Res. Lett.*, *42*, 765–772, doi:10.1002/2014GL062782.

Received 18 DEC 2014
Accepted 9 JAN 2015
Accepted article online 14 JAN 2015
Published online 10 FEB 2015

# How ocean waves rock the Earth: Two mechanisms explain microseisms with periods 3 to 300 s

**Fabrice Ardhuin[1,2], Lucia Gualtieri[3], and Eléonore Stutzmann[3]**

[1]Ifremer, Laboratoire d'Océanographie Spatiale, Brest, France, [2]Laboratoire de Physique des Oceans, CNRS-Ifremer-UBO-IRD, Brest, France, [3]Institut de Physique du Globe, PRES Sorbonne Paris-Cité, Paris, France

**Abstract** Microseismic activity, recorded everywhere on Earth, is largely due to ocean waves. Recent progress has clearly identified sources of microseisms in the most energetic band, with periods from 3 to 10 s. In contrast, the generation of longer-period microseisms has been strongly debated. Two mechanisms have been proposed to explain seismic wave generation: a primary mechanism, by which ocean waves propagating over bottom slopes generate seismic waves, and a secondary mechanism which relies on the nonlinear interaction of ocean waves. Here we show that the primary mechanism explains the average power, frequency distribution, and most of the variability in signals recorded by vertical seismometers, for seismic periods ranging from 13 to 300 s. The secondary mechanism only explains seismic motions with periods shorter than 13 s. Our results build on a quantitative numerical model that gives access to time-varying maps of seismic noise sources.

## 1. Introduction

Ocean waves provide most of the energy that feeds the continuous vertical oscillations of the solid Earth. In these, three period bands are usually identified. The hum contains periods longer than 30 s, and the primary and secondary peaks are centered around 15 and 5 s, respectively. Motions in all three bands are recorded everywhere on our planet [*Webb*, 1998; *Nishida*, 2013] and can provide information on both the solid Earth structure [*Shapiro et al.*, 2005], the ocean wave climate over the past century [*Bernard*, 1990; *Grevemeyer et al.*, 2000], and the properties of short-period ocean waves [*Farrell and Munk*, 2010]. Yet the use of seismic data is limited because where and how ocean waves rock the Earth is not known, in particular for the hum. The hum is the least understood part of Earth's oscillations. Recently discovered in seismometer records [*Nawa et al.*, 1998; *Suda et al.*, 1998], it has been associated with ocean waves for periods shorter than 300 s [*Tanimoto*, 2005; *Rhie and Romanowicz*, 2004; *Bromirski*, 2009; *Nishida*, 2013]. For any period, a Fourier analysis of the motions in the solid Earth and ocean layer shows that the transfer of energy from ocean waves to seismic waves is significant if ocean wave motions match both the wavelength and periods, and hence the speed, of seismic waves [*Hasselmann*, 1963]. This necessary matching of the speeds of different wave trains applies to all sorts of wave motions [*Hasselmann*, 1966], for example, the generation of atmospheric waves by tsunamis [e.g., *Artru et al.*, 2005]. Both primary and secondary mechanisms can be the matchmakers between slow ocean waves and much faster seismic waves. Without any of these two mechanisms, ocean waves propagating over a flat bottom only produce pressure oscillations in the water, at the frequency and wave number of the ocean waves, hence distinct from seismic waves. The crust deformation under such a pressure field is proportional to the local ocean wave amplitude and is known as compliance [e.g., *Crawford et al.*, 1991] and does propagate like seismic waves.

The secondary mechanism is best known, and corresponds to the nonlinear interaction of pairs of ocean wave trains with frequencies $f_1$ and $f_2$ and wave number vectors $\mathbf{k}_1$ and $\mathbf{k}_2$. It gives pressure patterns with sum and difference frequencies $f_1 \pm f_2$, wave numbers $\mathbf{k}_1 \pm \mathbf{k}_2$, and thus, phase velocities $C_s = 2\pi|f_1 \pm f_2|/|\mathbf{k}_1 \pm \mathbf{k}_2|$. We will not consider the difference interactions, which have been proposed in other studies [*Uchiyama and McWilliams*, 2008; *Traer and Gerstoft*, 2014], because only the sum interactions can yield velocities matching those of seismic waves [*Hasselmann*, 1963; *Webb*, 2008] (see also supporting information Text S1). With the secondary mechanism, velocity matching occurs for nearly opposing directions and nearly equal periods (Figure 1a).

In that case, seismic waves have a frequency that is twice the ocean wave frequency [*Longuet-Higgins*, 1950; *Hasselmann*, 1963; *Ardhuin and Herbers*, 2013]. That secondary mechanism explains the most energetic

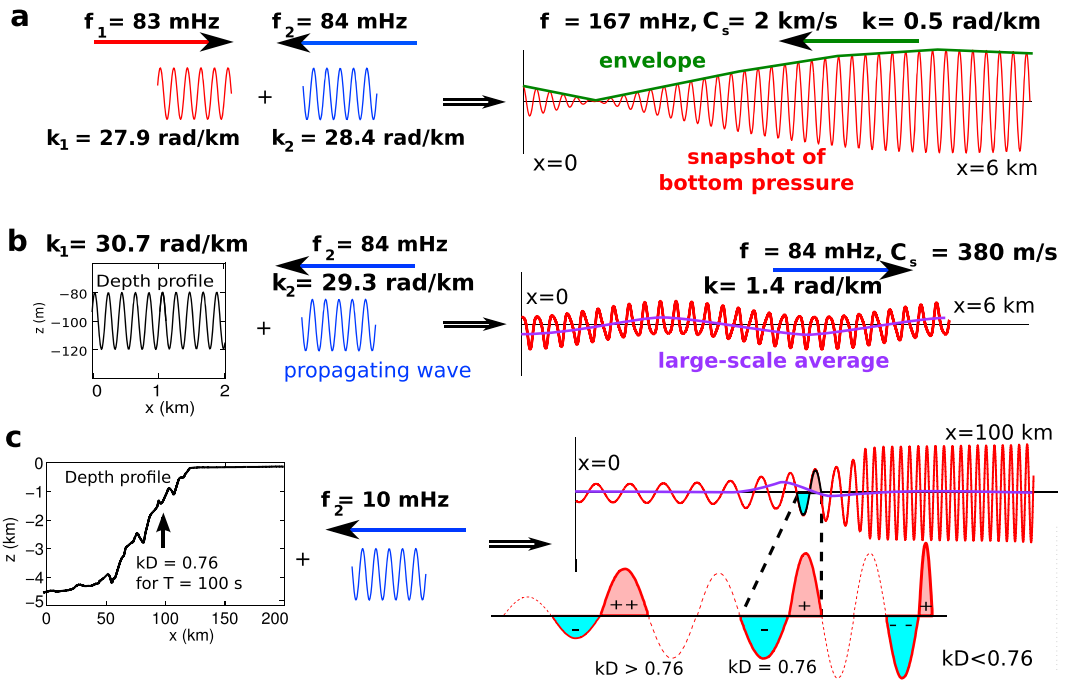


**Figure 1.** The two mechanisms that produce seismic noise. (a) In the secondary mechanism, opposing waves produce wave groups with fast traveling envelopes, in green. The second-order surface pressure (in red) is proportional to the surface velocity squared; hence, it contains Fourier components that have the same speed as the envelope. (b) The most simple case of the primary mechanism involves a wave with wave number $\mathbf{k}_2$ propagating over a sinusoidal bottom profile with almost the same wave number $\mathbf{k}_1$. The result is a large-scale oscillation of the bottom pressure, here in purple. As $k = \mathbf{k}_1 - \mathbf{k}_2$ goes to zero, the wavelength and speed of that oscillation go to infinity. (c) A realistic depth profile $D(x)$ contains all possible wavelengths, giving rise to pressure patterns with all possible speeds. The large-scale average of this pressure has a phase which changes sign where $kD = 0.76$, which is where the effect of an increase in wave amplitude toward shallow water is exactly compensated by the effect of a reduction in wavelength. Here the amplitude of the large-scale average was exaggerated for readability. Our choice of an infragravity wave propagating from the shoreline to open ocean corresponds to the most energetic hum sources off west coasts. In Figures 1b and 1c the time series of pressure at each point is a sinusoid.

seismic band with typical periods of 3 to 10 s [*Kedar et al.*, 2008; *Ardhuin et al.*, 2011; *Stutzmann et al.*, 2012; *Gualtieri et al.*, 2013]. At these periods, there is still a debate on the amplitude of the waves transmitted from the oceanic waveguide to the continental crust [e.g., *Obrebski et al.*, 2012; *Bromirski et al.*, 2013], which may vary with the shape of each continental margin.

In the primary mechanism, the bottom topography is like a frozen wave train, with $f_1 = 0$, but it contains wave numbers $\mathbf{k}_1$ that can take any value. Bottom interference with ocean waves of frequency $f_2$ and wave numbers $\mathbf{k}_2$ gives energy in the bottom pressure spectrum at the same period as the ocean waves (Figures 1b and 1c) but at wave numbers $\mathbf{k}_1 \pm \mathbf{k}_2$, which can match seismic wavelengths. This mechanism was invoked by *Hasselmann* [1963] to explain the "primary microseism" peak, with periods usually between 10 and 20 s. The only test of this theory considered periods around 20 s, 6 days of data for a single location [*Hasselmann*, 1963], and a constant bottom slope that was adjusted to fit seismic observations.

The generation of hum (30 to 300 s) by the primary or the secondary mechanism has been controversial [e.g., *Rhie and Romanowicz*, 2004; *Tanimoto*, 2006; *Webb*, 2007, 2008; *Nishida*, 2013]. Here we focus on vertical motions which are dominated by Rayleigh waves, but horizontal motions corresponding to Love waves can also be very energetic [*Kurrle and Widmer-Schnidrig*, 2008]. *Saito* [2010] and *Fukao et al.* [2010] have shown how a distributed random array of bottom topographic features could generate both Rayleigh and Love waves, suggesting that bottom slopes can be important. Also, *Nishida* [2013, 2014] showed that the maximum hum acceleration around 10 mHz suggests a generation by infragravity waves of the same frequency.

Yet without global quantitative information on long-period ocean waves, and a poor resolution of source locations estimated from measurements, both primary and secondary mechanisms appeared plausible [*Bromirski*, 2009]. Now, with a numerical wave model extended to the infragravity frequencies by *Ardhuin et al.* [2014], we evaluate the seismic sources predicted by both mechanisms, for all periods, and we model the seismic energy of the fundamental mode of Rayleigh waves, recorded by vertical seismometers.

## 2. The Primary Mechanism for Realistic Ocean Bottom Profiles

Because the interaction of waves with a sloping bottom has received little theoretical attention, we recall here how pressure fluctuations appear at large wavelengths when short ocean waves propagate over a sloping bottom, following *Hasselmann* [1963] with minor corrections. Further details are given in the supporting information Text S1. For straight and parallel depth contours, only waves propagating nearly perpendicular to them are able to produce seismic wavelengths. When depth variations occur at scales much smaller than the seismic wavelength, the seismic source amplitude is proportional to the horizontal integral of the ocean bottom pressure field. Decomposing this integral into sums over pairs of neighboring wave trough and crest reveals a particular pattern (Figure 1c). For a monotone bottom slope, the ocean waves shorten and, assuming that the energy is conserved, the wave amplitude increases. Over half a wavelength, the integrated bottom pressure is reduced by the shorter wavelength, corresponding to a higher wave number $k$, but increased by the larger amplitude. For any wave period, these two opposing effects cancel exactly at the depth $D_0$ where $kD_0$ equals 0.76. In deeper water, the amplification dominates over the shortening, with a nearly constant phase shift of the average pressure relative to the local pressure. For shallower water, this phase shift changes sign. As a result, the large-scale averaged pressure field is an oscillating dipole around the depth $D_0$, with two poles that do not exactly cancel. For any period, the seismic sources correspond to pressure oscillations at scales of the seismic wavelength, much larger than the ocean wavelength. These sources are thus distributed around $D_0$, provided that bottom slopes are significant. For periods of 16, 50, 100, and 200 s, $D_0$ is 30, 300, 1200, and 4800 m, respectively.

Hence, for periods longer than 50 s, sources are mostly located around shelf breaks. For shorter periods, depth variations on the scale of the ocean wavelength can strongly amplify the seismic source (Figures 1b and S2). Small-scale topographic features on the shallow part of continental shelves are the likely dominant sources of the primary microseismic peak, for periods between 10 and 20 s. In the following applications, the effect of the ocean bottom shape is represented by an effective slope that we take constant at $s = 6\%$, based on calculations for a wide variety of depth profiles (see supporting information Text S1, equation (S21), and Figure S3). The seismic source power is proportional to $s$.

## 3. Numerical Modeling and Seismic Data Processing

Four consecutive steps yield modeled spectra of the vertical ground acceleration. First, from analyzed winds over the oceans, we compute ocean wave spectra, with a spatial resolution of half a degree in longitude and latitude [*Ardhuin et al.*, 2014]. The results of this first step are distributions of wave energy in frequency and direction, every 3 h, at each point of the spatial grid. From these, in a second step, we obtain power spectral densities of pressure in wave number and frequency space at the sea surface [*Hasselmann*, 1963; *Ardhuin and Herbers*, 2013] and bottom [*Ardhuin and Herbers*, 2013]. Third, these pressure spectra are converted into sources of seismic Rayleigh waves [*Longuet-Higgins*, 1950; *Hasselmann*, 1963; *Ardhuin and Herbers*, 2013]. Our fourth and last step is the propagation of the Rayleigh wave energy along great circles, accounting for geometrical spreading and seismic attenuation [*Ardhuin and Herbers*, 2013; *Stutzmann et al.*, 2012]. Details about assumptions and technical implementation can be found in the supporting information Text S1.

Our numerical wave model is a global configuration (78°S to 80°N) of the spectral model WAVEWATCH III in its version 5.01 [*Tolman et al.*, 2014]. This configuration has a spatial resolution of half a degree in longitude and latitude, and a spectral grid that contains 36 evenly spaced directions, and 58 frequencies exponentially distributed between 3.3 mHz and 0.72 Hz. The energy reflection coefficient $R^2$ is parameterized from the wave height, frequency, and the local shoreface slope $s_f$ [*Ardhuin and Roland*, 2012]. This parameterization has $R^2$ increasing with wave period and decreasing with wave height; here we assumed a constant slope $s_f = 10\%$, and $R^2$ is limited to a maximum value of 80%. This 80% is generally the value applied in the infragravity wave band. The reflected spectrum is defined as the maximum, and not the sum, of the

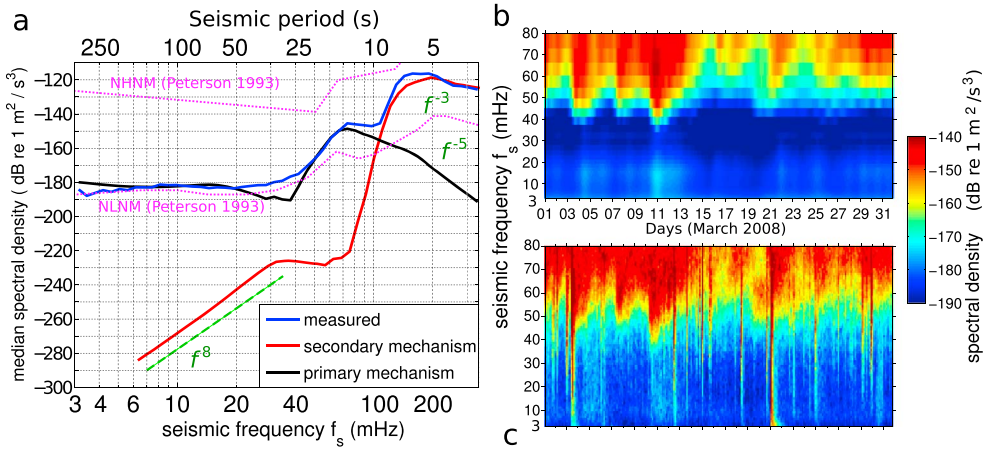


**Figure 2.** Measured spectra of the vertical ground acceleration, and modeled result for the primary and secondary mechanisms. (a) Median ground acceleration power spectra (LHZ channel) in March 2008 at the SSB seismic station (Geoscope Network) using records uncontaminated by earthquakes with magnitudes 5.6 and larger [*Ekström*, 2001]. The green dashed lines indicate different power law asymptotes. (b) Spectrogram of modeled ground acceleration and (c) measured spectrogram. Light blue to red vertical stripes correspond to earthquakes. The dotted magenta lines in (a) represent the New Low-Noise Model and New High-Noise Model of *Peterson* [1993], which is a familiar lower bound of microseismic activity.

reflection of incident waves and the expected local source of free infragravity waves. This procedure allows a smooth transition from the infragravity (IG) to the swell band, and the IG results are consistent with analyses of in situ data [*Ardhuin et al.*, 2014].

The output of this wave model includes standard parameters such as the significant wave height, used to verify the model against remote sensing data, and frequency-direction spectra of surface elevation $E(f,\theta)$ every 3 h at a selected list of points (10,000 points located every half degree along all the shorelines and the 300 m depth contour, including subgrid islands in the full resolution shoreline database compiled by *Wessel and Smith* [1996]). On the full model grid, we compute the second-order pressure spectrum at the sea surface and at near-zero seismic wave number.

These pressure spectra are transformed into seismic sources. These seismic sources are added and attenuated along great circles, including multiple orbits around the Earth, as described in the supporting information Text S1. That propagation of seismic energy is controlled by the product of the attenuation $Q$ and the group velocities $U$. For frequencies above 70 mHz we have used $Q = 240$ with $U = 1.8$ km/s, and a propagation coefficient $P = 1$, already adjusted to measurements at the SSB station [*Stutzmann et al.*, 2012]. For frequencies under 30 mHz and all seismic stations, $Q$ values are given by the QL6 model [*Durek and Ekstrom*, 1996], and we use seismic group velocities from the Preliminary Reference Earth Model [*Dziewonski and Anderson*, 1981]. Between 30 and 70 mHz the high-frequency and low-frequency values of $UQ$ are combined as shown in Figure S1. At 3 mHz this gives an $e$-folding distance of 30,000 km, and 9000 km at 7 mHz. Seismic data from the LHZ channel of the seismometers were obtained from Incorporated Research Institutions for Seismology (IRIS) Data Management Center and corrected for the instrument response. Spectra of the vertical displacement, every 3 h centered on the hour (e.g., from 10:30 UTC to 13:30 UTC), were given by the median of the spectra obtained with 1024 point Fourier transforms with half-overlapping windows. These spectra were automatically edited for earthquakes and glitches, removing all spectra which had a sudden relative increase or drop of power from one 3 h time step to the next, with a fixed threshold. Further removal of earthquake-contaminated records in Figures 2a and 3b uses the empirical editing criterion of *Ekström* [2001]. Namely, after each earthquake of magnitude greater than $M_w = 5.6$, a time segment was removed of duration

$$T = 2.5 + 40(M_w - 5.6) \quad (1)$$

where $T$ is in hours.

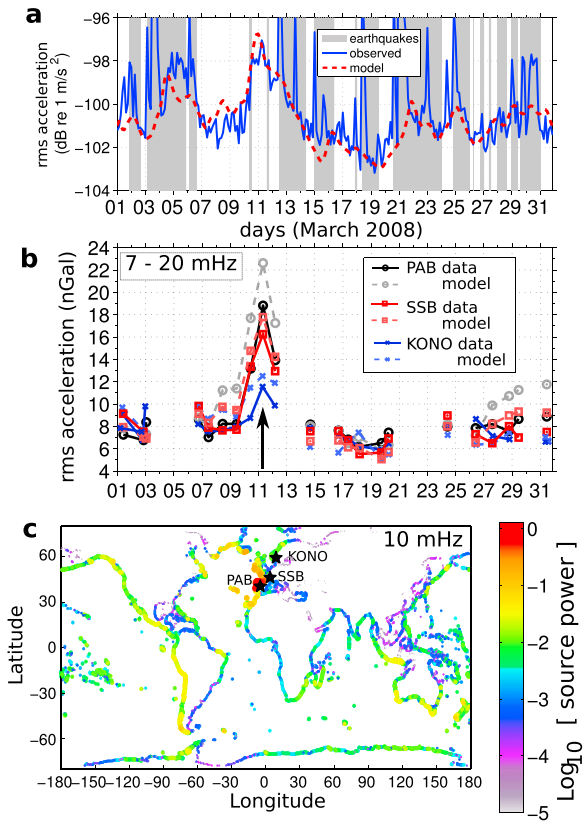


**Figure 3.** Noise time series and noise source distributions. (a) Measured root-mean-square vertical ground acceleration in the hum frequency band (7–20 mHz) at the SSB seismic station (Geoscope Network), obtained from the data and our hum model. Grey segments correspond to records contaminated by earthquakes with magnitudes $M_w \geq 5.6$ and larger. (b) Daily median root-mean-square acceleration without earthquake at the seismic stations SSB (Geoscope, France, in red), PAB (IU, Spain, in black), and KONO (IU, Norway, in blue). 1 nGal is $10^{-11}$ m s$^{-2}$. The arrow marks the noise event of 10–11 March, for which (c) the modeled seismic source distributions are shown. The source power shown here is the value of the spectral density of bottom pressure $F_p(\mathbf{k}_s = 0, f)/(\rho_w g)^2$, evaluated on 11 March at 00:00 UTC with equation (S22) given in the supporting information.

## 4. Results

We evaluated the primary and secondary mechanisms for the year 2008 at the locations of several seismic stations, with a first focus on the French Geoscope station SSB in March (Figure 2). As already shown [*Stutzmann et al.*, 2012; *Gualtieri et al.*, 2013], the secondary mechanism explains the main microseismic peak for periods between 3 and 10 s. For deep water waves, the predicted seismic acceleration power spectrum grows like the *n*th power of the frequency, with *n* close to 8 for periods longer than 25 s (Figure 2a and supporting information Text S1). This slope and the low spectral level are not consistent with measurements at periods longer than 13 s, contrary to previous estimates of deep water sources by *Webb* [2008]. *Ardhuin and Herbers* [2013] showed that for vanishing water depths compared to the ocean wave wavelength, the wave-induced pressure at the bottom exactly cancels the pressure at the surface. Because this bottom pressure was ignored by *Webb* [2007, 2008], it seemed possible that IG waves on the shelf could explain the measured hum levels. Taking bottom pressure into account here, we predict very low energy level at the lowest frequencies.

The primary mechanism, instead, reproduces the main features of the vertical seismic spectra, with a clear peak around 15 s, and a nearly constant acceleration spectrum from 50 s to 250 s (Figure 2a). A further verification of the theory and model is given by the time evolution of the hum amplitude (Figures 2b and 2c). The resemblance between model (Figure 2b) and measurements (Figure 2c) is clear at frequencies above 40 mHz, but lower frequencies are obscured by the many transient signatures of earthquakes. In particular, two events with magnitude $M_w = 6.9$ and $M_w = 7.1$ occurred on 3 March at 14:11 UTC and on 20 March at 22:33 UTC, according to the centroid moment tensor catalog [*Dziewonski et al.*, 1981; *Ekström et al.*, 2012]. The largest predicted hum event coincides with the strongest infragravity wave event, during the Johanna storm on 10–11 March 2008. That storm generated waves with a peak period of 16 s and significant wave height up to 12.8 m recorded at the Spanish buoy of Estaca de Bares, the highest value in the previous 12 years at that location. That storm also affected the entire Bay of Biscay [e.g., *Senechal et al.*, 2011]. In our model, the strongest source of infragravity waves is predicted along the North-West Spanish coast. The measured spectrogram in Figure 2c exhibits higher energy around 10 mHz at the time of this storm, extending over 36 h. This long duration is not compatible with the expected decay from the largest recent earthquake, a $M_w = 5.6$ event at 9:43 UTC on 10 March. We thus conclude that the measured seismic activity on 11 March around 00:00 UTC corresponds to the modeled infragravity waves and hum caused by the storm.

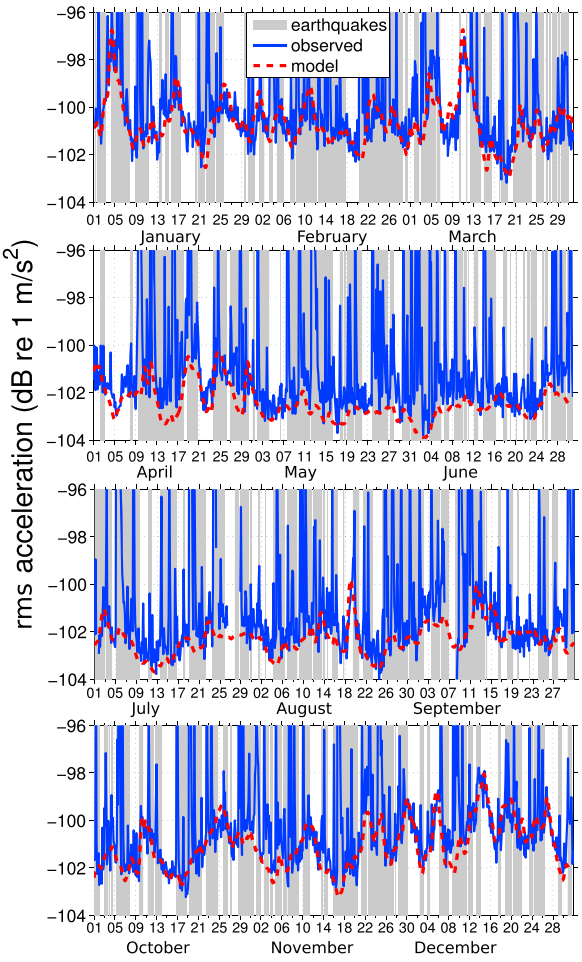


**Figure 4.** Same as Figure 3a, for the full year 2008: measured root-mean-square vertical ground acceleration in the hum frequency band (7–20 mHz) at the SSB seismic station (Geoscope Network), obtained from the data and our hum model, every 3 h. Grey segments correspond to records contaminated by earthquakes with magnitudes $M_w = 5.6$ and larger, according to *Ekström* [2001].

We performed a more quantitative analysis by integrating the acceleration around 80 s period (7 to 20 mHz), the peak of the predicted hum. The hum model provides an accurate lower bound of the seismic record when earthquake activity is low (Figure 3a). We estimated the root-mean-square acceleration for each 3 h record, and the median of these for each day, excluding records contaminated by earthquakes with magnitude $M_w = 5.6$ and larger, as described above [see also *Ekström*, 2001]. Results of this processing are shown in Figure 3b and extended to other seismic stations. The model reproduces the higher-hum energies during events that are strongest and closest to the seismic station, with a decrease in amplitude from station PAB in Spain, to KONO in Norway (Figure 3b). The infragravity bursts originate at the shoreline when long-period swells arrive there, typically in the eastern part of ocean basins. These infragravity waves propagate offshore from east to west [*Rawat et al.*, 2014], and hum sources are generally lower to the west of ocean basins (Figure 3c).

Model and observations have a similar decrease of hum amplitude by a factor 3 between the peak on 11 March, and the low level on March 19. Thus, observations are consistent with the linear dependence of the hum with infragravity wave height predicted by the primary mechanism. This consistency persists for the entire year (Figure 4). The second largest event of the year occurs on 5 and 6 January, with a strong infragravity wave event in the Gulf of Cadiz, described by *Rawat et al.* [2014].

Because IG waves produce seismic energy over bottom slopes, provided that the depth is shallow enough, mid-oceanic ridges or seamounts [*Fukao et al.*, 2010] may also be significant noise sources for periods larger than 100 s. When considering the average pressure across the mid-Atlantic ridge, we found effective slopes typically 10–100 times smaller than along shelf breaks (Figure S4). A quantitative statistical treatment of seamounts, such as proposed by *Saito* [2010] and *Fukao et al.* [2010] will be needed to determine the relative contributions of shelf topography, shelf break, mid-oceanic ridges, and seamounts.

## 5. Conclusion

Combining the correction for shallow water effects given by *Ardhuin and Herbers* [2013] for seismic noise generation by ocean waves, and an extension of a numerical ocean wave model for periods up to 300 s [*Ardhuin et al.*, 2014], we have shown that the nonlinear interaction of nearly opposing wave trains is a significant source of microseisms for periods shorter than 13 s and is negligible for longer periods. Waves propagating over a sloping bottom can generate the observed microseisms at periods from 13 to 300 s. Together, the two mechanisms provide a realistic model of the full microseism spectrum of Rayleigh waves,

recorded on vertical seismometers. An important prediction is that most hum sources, with periods 50 to 300 s, are located along the shelf breaks, and are generated by ocean waves of the same period. More work will be needed to expand the present analysis to Love waves and investigate the model-data discrepancies between 20 and 50 mHz. The seismic energy released in this process varies by up to 7 dB on the scale of a few days, associated with predictable infragravity wave events caused by long-period swells. A broadband numerical modeling of both ocean and seismic waves, as described here, should be accurate enough to guide the analysis of seismometer data for Earth-monitoring and tomographic studies.

**Acknowledgments**

F.A. is supported by European Research Council grant IOWAGA 240009, Labex Mer via grant ANR-10-LABX-19-01, and CNES under the SWOT preparation program. L.G. acknowledges the financial support of QUEST Initial Training Network funded within the EU Marie Curie Program. All seismic data were obtained from GEOSCOPE and IRIS data centers. The wave model code can be obtained from NOAA/NCEP, and the wind forcing fields are provided by ECMWF. The wave model results and reading tools can be found at http://tinyurl.com/iowagaftp/HINDCAST/OTHER_RUNS/GLOBAL_IG_36DIR.

The Editor thanks three anonymous reviewers for their assistance in evaluating this paper.

## References

Ardhuin, F., and T. H. C. Herbers (2013), Noise generation in the solid Earth, oceans and atmosphere, from nonlinear interacting surface gravity waves in finite depth, *J. Fluid Mech.*, *716*, 316–348.

Ardhuin, F., and A. Roland (2012), Coastal wave reflection, directional spreading, and seismo-acoustic noise sources, *J. Geophys. Res.*, *117*, C00J20, doi:10.1029/2011JC007832.

Ardhuin, F., E. Stutzmann, M. Schimmel, and A. Mangeney (2011), Ocean wave sources of seismic noise, *J. Geophys. Res.*, *116*, C09004, doi:10.1029/2011JC006952.

Ardhuin, F., A. Rawat, and J. Aucan (2014), A numerical model for free infragravity waves: Definition and validation at regional and global scales, *Ocean Modell.*, *77*, 20–32.

Artru, J., V. Ducic, H. Kanamori, P. Lognonn'e, and M. Murakami (2005), Ionospheric detection of gravity waves induced by tsunamis, *Geophys. J. Int.*, *160*, 840–848, doi:10.1111/j.1365-246X.2005.02552.x.

Bernard, P. (1990), Historical sketch of microseisms from past to future, *Phys. Earth Planet. Inter.*, *63*, 145–150.

Bromirski, P. D. (2009), Earth vibrations, *Science*, *324*, 1026–1027, doi:10.1126/science.1171839.

Bromirski, P. D., R. A. Stephen, and P. Gerstoft (2013), Are deep-ocean-generated surface-wave microseisms observed on land?, *J. Geophys. Res. Solid Earth*, *118*, 3610–3629, doi:10.1002/jgrb.50268.

Crawford, W. C., S. C. Webb, and J. A. Hildebrand (1991), Seafloor compliance observed by long-period pressure and displacement measurements, *J. Geophys. Res.*, *103*(B5), 9895–9916.

Durek, J., and G. Ekstrom (1996), A radial model of anelasticity consistent with long-period surface-wave attenuation, *Bull. Seismol. Soc. Am.*, *86*, 144–158.

Dziewonski, A. M., and D. L. Anderson (1981), Preliminary reference earth model, *Phys. Earth Planet. Inter.*, *25*(4), 297–356.

Dziewonski, A. M., T.-A. Chou, and J. H. Woodhouse (1981), Determination of earthquake source parameters from waveform data for studies of global and regional seismicity, *J. Geophys. Res.*, *86*(2), 2825–2852, doi:10.1029/JB086iB04p02825.

Ekström, G. (2001), Time domain analysis of Earth's long-period background seismic radiation, *J. Geophys. Res.*, *106*(B11), 26,483–26,493.

Ekström, G., M. Nettles, and A. M. Dziewonski (2012), The global CMT project 2004–2010: Centroid-moment tensors for 13,017 earthquake, *Phys. Earth Planet. Inter.*, *86*(2), 200–201, doi:10.1016/j.pepi.2012.04.002.

Farrell, W. E., and W. Munk (2010), Booms and busts in the deep, *J. Phys. Oceanogr.*, *40*(9), 2159–2169.

Fukao, Y., K. Nishida, and N. Kobayashi (2010), Seafloor topography, ocean infragravity waves, and background Love and Rayleigh waves, *J. Geophys. Res.*, *115*, B04302, doi:10.1029/2009JB006678.

Grevemeyer, I., R. Herber, and H.-H. Essen (2000), Microseismological evidence for a changing wave climate in the northeast Atlantic Ocean, *Nature*, *408*, 349–351.

Gualtieri, L., E. Stutzmann, Y. Capdeville, F. Ardhuin, M. Schimmel, A. Mangeney, and A. Morelli (2013), Modelling secondary microseismic noise by normal mode summation, *Geophys. J. Int.*, *193*, 1732–1745, doi:10.1093/gji/ggt090.

Hasselmann, K. (1963), A statistical analysis of the generation of microseisms, *Rev. Geophys.*, *1*(2), 177–210.

Hasselmann, K. (1966), Feynman diagrams and interaction rules of wave-wave scattering processes, *Rev. Geophys.*, *4*(1), 1–32.

Kedar, S., M. Longuet-Higgins, F. Webb, N. Graham, R. Clayton, and C. Jones (2008), The origin of deep ocean microseisms in the north Atlantic ocean, *Proc. R. Soc. London , Ser. A*, *464*, 777–793, doi:10.1098/rspa.2007.0277.

Kurrle, D., and R. Widmer-Schnidrig (2008), The horizontal hum of the Earth: A global background of spheroidal and toroidal modes, *Geophys. Res. Lett.*, *35*, L06304, doi:10.1029/2007GL033125.

Longuet-Higgins, M. S. (1950), A theory of the origin of microseisms, *Philos. Trans. R. Soc. London, Ser. A*, *243*, 1–35.

Nawa, K., N. Suda, Y. Fukao, T. Sato, Y. Aoyama, and K. Shibuya (1998), Incessant excitation of the Earth's free oscillations, *Earth Planets Space*, *50*, 3–8, doi:10.1029/2006GC001274.

Nishida, K. (2013), Earth's background free oscillations, *Annu. Rev. Earth Planet. Sci.*, *41*, 719–740.

Nishida, K. (2014), Source spectra of seismic hum, *Geophys. J. Int.*, *199*, 416–429.

Obrebski, M., F. Ardhuin, E. Stutzmann, and M. Schimmel (2012), How moderate sea states can generate loud seismic noise in the deep ocean, *Geophys. Res. Lett.*, *39*, L11601, doi:10.1029/2012GL051896.

Peterson, J. (1993), Observations and modeling of seismic background noise, *U.S. Geol. Surv. Tech. Rep., 93-322*, pp. 1–95.

Rawat, A., F. Ardhuin, V. Ballu, W. Crawford, C. Corela, and J. Aucan (2014), Infra-gravity waves across the oceans, *Geophys. Res. Lett.*, *41*, 7957–7963.

Rhie, J., and B. Romanowicz (2004), Excitation of Earth's continuous free oscillations by atmosphere-ocean-seafloor coupling, *Nature*, *431*, 552–556, doi:10.1038/nature02942.

Saito, T. (2010), Love-wave excitation due to the interaction between a propagating ocean wave and the sea-bottom topography, *Geophys. J. Int.*, *182*, 1515–1523.

Senechal, N., et al. (2011), The ECORS-Truc Vert 2008 field experiment: Extreme storm conditions over a three-dimensional morphology system in a macro-tidal environment, *Ocean Dyn.*, *61*, 2073–2098, doi:10.1007/s10236-011-0472-x.

Shapiro, N. M., M. Campillo, L. Stehly, and M. H. Ritzwoller (2005), High-resolution surface-wave tomography from ambient seismic noise, *Science*, *307*, 1615–1617, doi:10.1111/j.1365-246X.2006.03240.x.

Stutzmann, E., M. Schimmel, and F. Ardhuin (2012), Modeling long-term seismic noise in various environments, *Geophys. J. Int.*, *191*, 707–722, doi:10.1111/j.1365-246X.2012.05638.x.

Suda, N., K. Nawa, and Y. Fukao (1998), Earths background free oscillations, *Science*, *279*, 2089–2091.

Tanimoto, T. (2005), The oceanic excitation hypothesis for the continuous oscillations of the Earth, *Geophys. J. Int.*, *160*, 276–288, doi:10.1111/j.1365-246X.2004.02484.x.

Tanimoto, T. (2006), Excitation of normal modes by non-linear interaction of ocean waves, *Geophys. J. Int.*, *168*, 571–582, doi:10.1111/j.1365-246X.2008.03801.x.

Tolman, H. L., et al. (2014), User manual and system documentation of WAVEWATCH-III$^{TM}$ version 4.18, *NOAA/NWS/NCEP/MMAB Tech. Rep.*, *316*, 194 pp.

Traer, J., and P. Gerstoft (2014), A unified theory of microseisms and hum, *J. Geophys. Res. Solid Earth*, *119*, 3317–3339, doi:10.1002/2013JB010504.

Uchiyama, Y., and J. C. McWilliams (2008), Infragravity waves in the deep ocean: Generation, propagation, and seismic hum excitation, *J. Geophys. Res.*, *113*, C07029, doi:10.1029/2007JC004562.

Webb, S. C. (1998), Broadband seismology and noise under the ocean, *Rev. Geophys.*, *36*, 105–142.

Webb, S. C. (2007), The Earth's "hum" is driven by ocean waves over the continental shelves, *Nature*, *445*, 754–756, doi:10.1038/nature05536.

Webb, S. C. (2008), The Earth's "hum": The excitation of Earth normal modes by ocean waves, *Geophys. J. Int.*, *174*, 542–566, doi:10.1111/j.1365-246X.2008.03801.x.

Wessel, P., and W. H. F. Smith (1996), A global self-consistent hierarchical, high-resolution shoreline database, *J. Geophys. Res.*, *101*, 8741–8743.